Three-dimensional local anisotropy of velocity fluctuations in the solar wind

Andrea Verdini, Roland Grappin, Olga Alexandrova, L. Franci, S. Landi, L. Matteini, E. Papini

Monthly Notices
of the
ROYAL ASTRONOMICAL SOCIETY

MNRAS **486,** 3006–3018 (2019)
Advance Access publication 2019 April 13

doi:10.1093/mnras/stz1041

Three-dimensional local anisotropy of velocity fluctuations in the solar wind

Andrea Verdini [1★] R. Grappin,[2] O. Alexandrova,[3★] L. Franci,[4] S. Landi,[1] L. Matteini[3★] and E. Papini[1]

[1]*Dipartimento di Fisica e Astronomia, Universitá di Firenze, 50019 Firenze, Italy*
[2]*Laboratoire de Physique des Plasmas, Ecole Polytechnique, 91128 Palaiseau, France*
[3]*LESIA, Observatoire de Paris, Université PSL, CNRS, Sorbonne Université, Univ. Paris Diderot, Sorbonne Paris Cité, 92195 Meudon, France*
[4]*School of Physics and Astronomy, Queen Mary University of London, E1 4NS London, UK*

Accepted 2019 April 8. Received 2019 April 8; in original form 2019 January 17

ABSTRACT

We analyse velocity fluctuations in the solar wind at magneto-fluid scales in two data sets, extracted from *Wind* data in the period 2005–2015, that are characterized by strong or weak expansion. Expansion affects measurements of anisotropy because it breaks axisymmetry around the mean magnetic field. Indeed, the small-scale three-dimensional local anisotropy of magnetic fluctuations (δB) as measured by structure functions (SF_B) is consistent with tube-like structures for strong expansion. When passing to weak expansion, structures become ribbon-like because of the flattening of SF_B along one of the two perpendicular directions. The power-law index that is consistent with a spectral slope $-5/3$ for strong expansion now becomes closer to $-3/2$. This index is also characteristic of velocity fluctuations in the solar wind. We study velocity fluctuations (δV) to understand if the anisotropy of their structure functions (SF_V) also changes with the strength of expansion and if the difference with the magnetic spectral index is washed out once anisotropy is accounted for. We find that SF_V is generally flatter than SF_B. When expansion passes from strong to weak, a further flattening of the perpendicular SF_V occurs and the small-scale anisotropy switches from tube-like to ribbon-like structures. These two types of anisotropy, common to SF_V and SF_B, are associated with distinct large-scale variance anisotropies of δB in the strong- and weak-expansion data sets. We conclude that SF_V show anisotropic three-dimensional scaling similar to SF_B, with however systematic flatter scalings, reflecting the difference between global spectral slopes.

Key words: turbulence – solar wind.

1 INTRODUCTION

The solar wind is a turbulent plasma that expands spherically in the heliosphere, with magnetic and velocity fluctuations having a power-law spectrum on several decades in frequency (e.g. Bruno & Carbone 2013 for a review). Above proton scales, where magnetohydrodynamics (MHD) is a good description of the plasma, the power-law index of magnetic fluctuations is on average $-5/3$, while velocity fluctuations have a flatter spectrum with an Iroshinikov–Kraichnan index, $-3/2$ (e.g. Podesta, Roberts & Goldstein 2007; Salem et al. 2009; Tessein et al. 2009). The latter does not vary with properties of solar wind streams, while the magnetic index approaches a value $-3/2$ in strongly Alfvénic intervals (Chen et al. 2013) (Alfvénic intervals are those with a strong correlation between magnetic and velocity fluctuations). The existence of different spectral indices shows that, on the one hand, homogenous MHD turbulence is a valid framework to interpret solar wind fluctuations, and, on the other hand, that some physical mechanisms beyond homogenous MHD turbulence may be needed to reproduce the observed properties. In fact, in homogenous incompressible MHD a cascaded quantity is associated with the existence of an ideally conserved quantity, namely the total (kinetic plus magnetic) energy. Since magnetic and kinetic energy are not conserved separately, there is no reason to expect different power laws for their spectra (we will come back on this point in the discussion), yet different spectral index are observed.

Theories generally assume the same spectral index for the two fields (e.g. Goldreich & Sridhar 1995; Boldyrev 2005, 2006),

★ E-mail: andrea.verdini@unifi.it (AV); olga.alexandrova@obspm.fr (OA); lorenzo.matteini@obspm.fr (LM)

while numerical works either focus on the spectrum of the total energy or the magnetic energy (e.g. Müller, Biskamp & Grappin 2003; Beresnyak & Lazarian 2006; Mason, Cattaneo & Boldyrev 2006, 2008; Grappin & Muller 2010; Perez et al. 2012; Beresnyak 2015) or, when studying magnetic and velocity spectra, they obtain different spectral indices that do not match the observed values (e.g. Cho & Vishniac 2000; Milano et al. 2001; Muller & Grappin 2005). There are few numerical exceptions that report the spectral indices −5/3 and −3/2 for magnetic and velocity fluctuations, respectively: decaying two-dimensional (2D) hybrid simulations (Franci et al. 2015a, b), decaying 2D Hall-MHD simulations (Papini et al. 2019), forced simulations of reduced MHD (Boldyrev et al. 2011), and decaying simulations of full three-dimensional (3D) MHD without guide field (Grappin, Müller & Verdini 2016). Such simulations have different governing equations (full MHD, reduced MHD, Hall MHD, or fluid electrons and particle in cell protons), indicating that separate spectral indices can be obtained in a rather general context. However they also have different large-scale dynamics (decaying or forcing) and different configurations (3D or 2D, with or without a mean field), which are not necessarily appropriate to describe solar wind turbulence that is expected to be 3D, decaying, and with a mean field of the order of the fluctuations. Although a spectral relation between the total energy and residual energy (the difference between magnetic and kinetic energies) is a promising approach (Grappin, Leorat & Pouquet 1983; Müller & Grappin 2004; Muller & Grappin 2005; Grappin et al. 2016), with the residual energy originating from current sheets formed in the cascade process (e.g. Matthaeus & Lamkin 1986), there is currently no explanation for the difference in spectral indices of the magnetic and velocity fluctuations. Note, finally, that when the mean field is absent, the total energy spectrum can have a slope −2, −5/3, or −3/2 depending on initial condition or forcing (Lee et al. 2010; Krstulovic, Brachet & Pouquet 2014): even for a conserved quantity the spectral index may be non-universal.

Solar wind turbulence is also anisotropic with respect to the mean-field direction. Most of the works deal with magnetic field fluctuations, possibly because of the high cadence of the *in situ* data and the association of strong currents with heating events (Osman et al. 2011, 2012). Again, measurements of anisotropy with respect to the mean field, either calculated at large scale (global anisotropy) or at each scale (local anisotropy), show features that are characteristic of homogeneous MHD turbulence with some noticeable exceptions.

To be more specific, when global anisotropy is computed on solar wind data, magnetic fluctuations have a stronger power in the field-perpendicular wavevectors than in the field-parallel wavevectors, as expected for a plasma threaded by a mean field (Montgomery & Turner 1981; Shebalin, Matthaeus & Montgomery 1983; Grappin 1986; Müller et al. 2003; Verdini et al. 2015). However, in fast streams, magnetic fluctuations possess also the so-called slab component, with most of the energy residing in field-aligned wavevectors (Matthaeus, Goldstein & Roberts 1990; Bieber, Wanner & Matthaeus 1996; Dasso et al. 2005; Weygand et al. 2009, 2011). This component has no stable counterpart in homogeneous MHD (Ghosh et al. 1998a,b but see Zank et al. 2017 for an explanation based on nearly incompressible MHD). However, it can be easily explained as the result of the (wrong) assumption of axisymmetry around the mean field for structures that are instead axisymmetric around the radial direction. In fact, a radial symmetry emerges naturally when the non-linear dynamics is slower than the expansion of the solar wind (Völk & Aplers 1973; Heinemann 1980; Grappin, Velli & Mangeney 1993; Verdini & Grappin 2016), and is compatible with measurements at large scales (Saur & Bieber 1999). Whether the radial axis stops to rule the anisotropy at small scales depends on the tendency of turbulence to become strong, in analogy to the switch from weak to strong turbulence in homogenous MHD (e.g. Verdini & Grappin 2012; Meyrand, Galtier & Kiyani 2016). For the solar wind, it is still unclear whether axisymmetry around the mean field is restored at proton scales (Hamilton et al. 2008; Narita et al. 2010; Lacombe, Alexandrova & Matteini 2017; Roberts, Narita & Escoubet 2017).

When local anisotropy is computed, the spectral index is found to vary with the angle θ_{BV} between the mean field and the sampling direction, which is the radial direction of the wind flow. Most of the studies analysed magnetic field data in fast streams (Horbury, Forman & Oughton 2008; Podesta 2009; Wicks et al. 2010, 2011; Wang et al. 2014) and obtained spectral indices that pass from −2 to −5/3 with increasing θ_{BV} angle. These results are consistent with the anisotropy of homogenous strong turbulence, which is regulated by the critical balance between the linear Alfvén time and the non-linear eddy turnover time (Goldreich & Sridhar 1995). Exceptions are found in the works by Luo & Wu (2010) and Wang et al. (2016). In the former, the spectral index in the perpendicular direction was closer to −3/2, a value predicted when magnetic and velocity fluctuations progressively align at small scales (Boldyrev 2005, 2006). Wang et al. (2016), instead, found a weaker field-parallel index (−1.75) by requiring the magnetic field direction to be stable at large scales. However this result is not completely understood. The stability requirement alone seems not sufficient to return a weaker parallel spectral index (see the analysis in Gerick, Saur & von Papen 2017), although it limits the intermittency in the analysed intervals. Removal of intermittency from data yields flatter parallel spectra (Wang et al. 2014), but the same procedure only affects perpendicular spectra in numerical simulations (Yang et al. 2017).

Relaxation of axisymmetry in the measurements of local anisotropy (3D anisotropy) revealed that structures have their largest dimension in the field-parallel direction and are axisymmetric around this axis only at small scales (Chen et al. 2012). At large scales, turbulent eddies have their largest dimension in the displacement direction, i.e. the direction perpendicular to the mean field and with a component along the fluctuation direction (the proper perpendicular direction is perpendicular to both the mean field and the fluctuation, see Fig. 1a, b). Numerical simulations of MHD turbulence with the Expanding Box Model (EBM, Velli, Grappin & Mangeney 1992; Grappin et al. 1993; Grappin & Velli 1996) allowed interpreting this unusual large-scale anisotropy as a consequence of the spherical expansion of the solar wind, which introduces a radial symmetry in the amplitude of magnetic field fluctuations, with radial fluctuations being less energetic than those transverse to the radial (see Dong, Verdini & Grappin 2014 for 3D simulations and Section 2 for an explanation based on the conservation of the magnetic flux).

In addition, there are indications that expansion can alter also the small-scale anisotropy. In fact, the above simulations (Verdini & Grappin 2015) also showed that the spectral indices in the perpendicular and displacement directions are the same when data are sampled in the radial direction, in agreement with observations (Chen et al. 2012), while they are different when sampling in directions transverse to the radial. These numerical results were partially confirmed by a two-spacecraft analysis (Vech & Chen 2016). Following these findings, Verdini et al. (2018a) computed the 3D local anisotropy of magnetic fluctuations in two data sets in which the effects of expansion are expected to be large and weak, respectively. For strong expansion they recovered the same

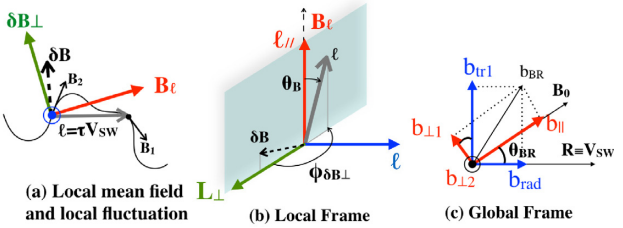

Figure 1. (a) From the measurements of magnetic fields at two different times, $\boldsymbol{B}_1$ and $\boldsymbol{B}_2$ (black arrows), separated by the lag τ, one obtains the local mean field $\boldsymbol{B}_\ell$ (red arrow) and the local fluctuation $\delta\boldsymbol{B}$ (black dashed arrow). The displacement direction (green arrow) lies in the plane defined by δB and B_ℓ and is perpendicular to the latter. The perpendicular direction (blue) completes the reference frame and is orthogonal to the plane of the figure. (b) The reference frame as obtained from the configuration on the left. The increment along the sampling direction is indicated with a grey arrow and its orientation in spherical coordinates is measured with the polar and azimuthal angles, θ_B, $\phi_{\delta B\perp}$, respectively. For purpose of illustration we choose the mean flow $\boldsymbol{V}_{sw}$ to be coplanar with $\boldsymbol{B}_1$ and $\boldsymbol{B}_2$ (the light-blue shaded plane), in the general case the vector $\boldsymbol{\ell}$ has a random orientation in the perpendicular plane where $\phi_{\delta\boldsymbol{B}\perp}$ is measured. (c) Relation between the radial-aligned and field-aligned reference frames (blue and red arrows, respectively). b_{BR} is the projection of the fluctuation in the BR plane containing the radial and large-scale mean-field directions that form an angle θ_{BR}.

anisotropy as in Chen et al. (2012), in agreement with axisymmetry at small scales, as predicted by the critical balance (Goldreich & Sridhar 1995). Instead, for weak expansion, they obtained different spectral indices in the perpendicular and displacement directions, i.e. non-axisymmetric structures similar to ribbons, an anisotropy predicted by Boldyrev (2005, 2006).

Velocity fluctuations have not been studied in such detail, possibly because of the lower resolution of plasma data, although vortical structures are ubiquitous in the solar wind (Perrone et al. 2016, 2017) and small-scale vorticity enhancements are shown to be co-spatial with preferential perpendicular heating of protons in 2D hybrid simulations (Franci et al. 2016). As a result, their anisotropy is less constrained. First, there is no measurement of the 3D anisotropy of velocity fluctuations. Second, the measurements of axisymmetric anisotropy yield contradictory results. On the one hand, by analysing a single fast stream in the ecliptic, Wicks et al. (2011) found angle-dependent power-law indices, the index decreasing monotonically from -2 to $-3/2$ when θ_{BV} passes from 0^o to 90^o. On the other hand, by averaging seven fast streams including the previous one, Wang et al. (2014) found that the index of velocity fluctuations was consistent with an angle-independent value of $-3/2$, although in some particular streams the field-parallel direction had an index -2. They also suggested that differences in velocity and magnetic anisotropy arise from intermittency. In fact, when intermittency was removed from the data they obtained similar and angle-independent indices for the magnetic and velocity fluctuations. This is at odds with earlier analysis of solar wind data and with recent numerical simulations. Salem et al. (2009) removed intermittency from *Wind* data and still obtained spectral indices of $-5/3$ and $-3/2$ for the magnetic and velocity fluctuations, respectively (although they did not consider the anisotropy with respect to the mean field). Upon removal of intermittency in direct numerical simulation of compressible MHD, Yang et al. (2017) found only small variations of the spectral index anisotropy, with indices being always the larger in the field-parallel direction.

In this work we extend the 3D analysis of local anisotropy of magnetic fluctuations (Chen et al. 2012; Verdini et al. 2018a) to velocity fluctuations, by analysing separately intervals with weak and strong expansion. In Section 2 we briefly describe the method used to construct the data sets and to analyse the anisotropy via second-order structure functions. In Section 3 we complement the characterization of the two data sets given in Verdini et al. (2018a). In Section 4.1 we present the results on the local anisotropy of magnetic and velocity fluctuations under the assumption of axisymmetry. We then show the 3D anisotropy of velocity fluctuations in Section 4.2. In Section 5 we summarize and discuss the results.

2 DATA AND METHOD OF ANALYSIS

We briefly describe the data and the method used in the analysis, more details can be found in Verdini et al. (2018a). We use data at 1au from instruments on *Wind* spacecraft in the period 2005–2015: magnetic field data at 3s resolution from MFI instrument (Lepping et al. 1995) and onboard ion moments at 3s resolution from 3DP/PESA-L (Lin et al. 1995). To separate intervals with weak and strong expansion we compute the ratio

$$E = \frac{b_{\rm tr}^2}{b_{\rm rad}^2} = \left.\frac{b_Y^2 + b_Z^2}{b_X^2}\right|_{\mathcal{T}\,=\,2\,\rm h}, \tag{1}$$

where (X, Y, Z) are the GSE coordinates (with X aligned with the radial direction), the subscripts *rad* and *tr* refer to the radial and transverse-to-the-radial components, and the fluctuations $b_{X,Y,Z}$ are obtained by subtracting a running average with a window of duration $\mathcal{T} = 2$ h from the original signal: $\boldsymbol{b} = \boldsymbol{B} - \langle\boldsymbol{B}\rangle_{\mathcal{T}}$. The two data sets contain intervals of at least 5 h that satisfy at each time the following criteria: the two data sets contain intervals of minimal duration that satisfy continuously for at least 5 h the following criteria:

$$2 < E < 10 \quad \text{strong-expansion data set,} \tag{2}$$

$$0 < E < 2 \quad \text{weak-expansion data set.} \tag{3}$$

Continuously means that the criterion must be satisfied at each time belonging to the interval, and not only on average in the interval, although we allow for out-of-bounds values of E on a duration of 1 min (see fig. 1 in Verdini et al. 2018a).

The relation between E and expansion is now briefly explained, more details can be found in Grappin & Velli (1996), Dong et al. (2014), Verdini & Grappin (2015), and Montagud-Camps, Grappin & Verdini (2018). For a spherically expanding flow, the conservation of magnetic flux imposes a weaker decay of transverse components of magnetic fluctuations compared to the radial one, $b_{\rm tr} \propto 1/R$ and $b_{\rm rad} \propto 1/R^2$. Assuming component isotropy close to the Sun ($b_Y \sim b_Z \sim b_X$ and so $E = 2$), one finds stronger transverse fluctuations at 1au, with $E > 2$. Note, however, that velocity fluctuations must satisfy the conservation of angular momentum, $u_{\rm tr} \propto 1/R$ and $u_{\rm rad} = const$, resulting in the opposite behaviour, i.e. a faster decay of transverse components. Any form of coupling between velocity and magnetic fluctuations has the effect of smearing out the anisotropy evaluated by E. For a strong linear Alfvénic coupling, all the components of velocity and magnetic fluctuations decay as $1/\sqrt{R}$, thus maintaining the value of E close to the Sun (e.g. Dong et al. 2014). Instead, when the non-linear coupling is strong, a component anisotropy with respect to the mean magnetic field direction develops (e.g. Oughton et al. 2016). At large scales (of the order of few hours in the solar wind) one expects the expansion time-scale to be shorter than the non-linear time-scale and the Alfvén time-scale, so that E is ruled by the conservation of magnetic flux. This is confirmed by numerical simulations of MHD turbulence

in 3D with a mean magnetic field of the order of the fluctuations. Without expansion and with an oblique mean field, $E \approx 2$ at all times, while in presence of expansion E increases monotonically with distance and does not depend much on the scale at which it is computed (Verdini & Grappin 2015). It should be noticed that requiring $E > 2$ to isolate intervals with strong expansion is only an approximate criterion, since the divergence-less condition of magnetic fluctuations contributes to such inequality as much as expansion in single spacecraft measurements (Vech & Chen 2016).

Although we will compute the local anisotropy of velocity structure functions, we define the local reference frame with respect to the local mean magnetic field and the local magnetic fluctuation as in Chen et al. (2012). For each pair of magnetic field $\boldsymbol{B}_1 = \boldsymbol{B}(t)$, $\boldsymbol{B}_2 = \boldsymbol{B}(t+\tau)$ separated by a time lag τ, the fluctuation is defined as

$$\delta\boldsymbol{B} = \boldsymbol{B}_1 - \boldsymbol{B}_2, \tag{4}$$

while the local mean field is given by

$$\boldsymbol{B}_l = 1/2(\boldsymbol{B}_1 + \boldsymbol{B}_2). \tag{5}$$

We choose the z-axis along the mean field, the x-axis along the local perpendicular displacement direction,

$$\delta\boldsymbol{B}_\perp \propto \boldsymbol{B}_l \times [\delta\boldsymbol{B} \times \boldsymbol{B}_l], \tag{6}$$

and the y-axis, the perpendicular direction, is orthogonal to both the fluctuation and the mean field (see Fig. 1a). We use a spherical polar coordinate system in which the radial vector $\boldsymbol{\ell}$ coincides with the solar wind flow direction, i.e. the sampling direction, and use the polar θ_B and azimuthal $\phi_{\delta B\perp}$ angles to measure its orientation with respect to the mean-field and the displacement directions, respectively (see Fig. 1b).

For each pair of points, the square of the velocity fluctuation is binned in this 3D coordinate system, and the velocity structure function is defined as

$$SF_i(\ell, \theta_B, \phi_{\delta B\perp}) = \left\langle \delta\boldsymbol{V}^2 \right\rangle_i = \left\langle |\boldsymbol{V}_1 - \boldsymbol{V}_2|^2 \right\rangle_i , \tag{7}$$

where we have indicated with $\langle ... \rangle_i$ an average on all increments computed in the interval i. We use 66 logarithmically spaced increments to measure the power level in the range 10^{-4} Mm^{-1} $< k <$ 1 Mm^{-1}, where $k = 1/\ell$ is the wavenumber obtained from the increment $\boldsymbol{\ell} = \tau \boldsymbol{V}_{SW}$. The sampling direction is given by the solar wind speed, $\boldsymbol{V}_{SW}$, which is the average of the first moment of the ion distribution computed in each interval, $\boldsymbol{V}_{SW} = \langle \boldsymbol{V} \rangle_i$ (using a local definition $\boldsymbol{V}_{SW}(\ell) = 1/2(\boldsymbol{V}_1 + \boldsymbol{V}_2)$ does not change the results). For the polar and azimuthal angles we use 5° bins to cover one quadrant only (any angle greater than 90° is reflected below 90°).

To obtain an *SF* for a given data set, before averaging among intervals we normalize each structure function, $SF_i(\ell, \theta_B, \phi_{\delta B\perp})$, by the energy of velocity fluctuations at a scale $\ell^* = 100$ Mm, which is in the middle of the power-law range of their spectrum. The energy is obtained by averaging over angles

$$S_i(\ell^*) = \sum_{\theta_B, \phi_{\delta B\perp}} w_i SF_i \tag{8}$$

with weights given by

$$w_i = N_i(\ell, \theta_B, \phi_{\delta B\perp})/N_i(\ell) , \tag{9}$$

where $N_i(\ell) = \sum_{\theta_B, \phi_{\delta B\perp}} N_i(\ell, \theta_B, \phi_{\delta B\perp})$. The average among intervals is weighted with the relative count in each bin, so that the structure function is given by

$$SF(\ell, \theta_B, \phi_{\delta B\perp}) = \langle w_i SF_i / S_i(\ell^*) \rangle_i \tag{10}$$

with weights

$$w_i = N_i(\ell, \theta_B, \phi_{\delta B\perp})/N(\ell, \theta_B, \phi_{\delta B\perp}). \tag{11}$$

From the recorded values of SF_i we can also compute the axisymmetric *SF* by averaging along the azimuthal angle $\phi_{\delta B\perp}$. The axisymmetric *SF* will be used for comparison with previous works and is obtained as

$$SF(\ell, \theta_B) = \left\langle \sum_{\phi_{\delta B\perp}} \left[w_i SF_i / S_i(\ell^*) \right] \right\rangle_i , \tag{12}$$

with weights given by

$$w_i = N_i(\ell, \theta_B, \phi_{\delta B\perp})/N(\ell, \theta_B), \tag{13}$$

in which we have defined $N(\ell, \theta_B) = \sum_{i, \phi_{\delta B\perp}} N_i$.

We will also compute the *raw* axisymmetric *SF* that is obtained in a similar way but without applying any normalization to the SF_i that belong to the same data set, i.e.

$$SF(\ell, \theta_B) = \left\langle \sum_{\phi_{\delta B\perp}} [w_i SF_i] \right\rangle_i \tag{14}$$

with w_i in equation (13). This raw *SF* will be used to evaluate the signal-to-noise ratio in velocity structure functions. We will also show the axisymmetric *SF* for magnetic fluctuations, SF_B, which is obtained by collecting the power $\langle |\boldsymbol{B}_1 - \boldsymbol{B}_2|^2 \rangle_i$ in equation (7). This power is then used in equation (8) to compute the magnetic energy for the (eventual) normalization.

3 DATA SET PROPERTIES

3.1 Implication of the selection criterion

The ratio E, used to separate weak-expansion and strong-expansion intervals, introduces a bias on the mean magnetic field direction and on the relative magnitude of the components of magnetic fluctuations (component anisotropy or variance anisotropy). To see how, let us rewrite the ratio $E = b_{\rm tr}^2/b_{\rm rad}^2$ in the reference frame attached to the mean magnetic field direction, assumed to form an angle θ_{BR} with the radial direction, as represented in Fig. 1c. Indicating the components of fluctuations in this reference frame with $(b_\parallel, b_{\perp 1}, b_{\perp 2})$, with $b_{\perp 1}$ lying in the *BR* plane, we have

$$E = \frac{b_{\rm tr1}^2 + b_{\perp 2}^2}{b_{\rm rad}^2} = \frac{\left(b_\parallel \sin\theta_{BR} + b_{\perp 1}\cos\theta_{BR}\right)^2 + b_{\perp 2}^2}{\left(b_\parallel \cos\theta_{BR} + b_{\perp 1}\sin\theta_{BR}\right)^2}$$

$$\approx \frac{(b_{\perp 2}/b_{\perp 1})^2 + \cos^2\theta_{BR}}{\sin^2\theta_{BR}}, \tag{15}$$

where in the last equality we have assumed $b_\parallel \ll b_{\perp 1}, b_{\perp 2}$, i.e. a weak magnetic compressibility. It is worth mentioning that this strong inequality is used here as a simplification assumption, but it does not alter the final results (see below). In the solar wind one rather finds $b_\parallel \lesssim 1/2 b_\perp$, see for example Fig. 3a. We recall that incompressible MHD turbulence can maintain variance isotropy ($b_\parallel \sim b_\perp$), while $b_\parallel < b_\perp$ is an asymptotic stated of decaying weakly compressible MHD turbulence (see Matthaeus et al. 1996; Oughton et al. 2016). The function is periodic with period π and its form (equation 16) is shown in the left-hand panel of Fig. 2 for two values of the parameter $b_{\perp 1}/b_{\perp 2} = 2, 0.8$. This parameter also set the minimum, $E_{\rm min} = b_{\perp 2}^2/b_{\perp 1}^2$, which is always located at $\theta_{BR} = \pi/2$: the larger the ratio, the smaller is the minimum. With the chosen parameters that are indicated in the figure, $E_{\rm min} = 0.25, 1.56$.

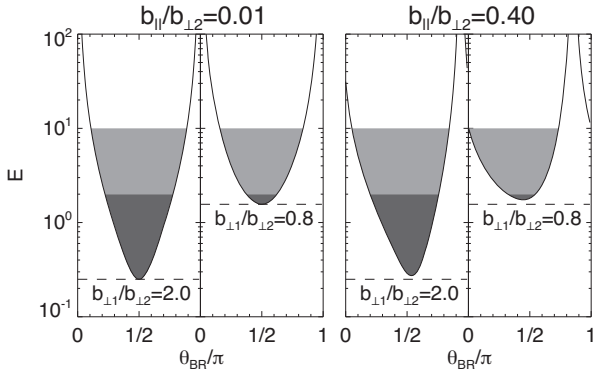

Figure 2. The ratio E as a function of θ_{BR} (see equation 15) with $b_{\perp1}/b_{\perp2} = 2$, 0.8. The horizontal dashed line is the value $b^2_{\perp2}/b^2_{\perp1}$ that corresponds to the minimum of E at $\theta_{BR} = \pi/2$ only for small $b_\parallel/b_{\perp2}$ (0.01 in the left-hand panel). When $b_\parallel/b_{\perp2}$ increases (0.4 in the right-hand panel) the function becomes asymmetric, the minimum shifts to larger values and angles, while the asymptotes move to smaller angles. The light and dark grey areas correspond to the values of E that determine the strong- and weak-expansion data sets, respectively.

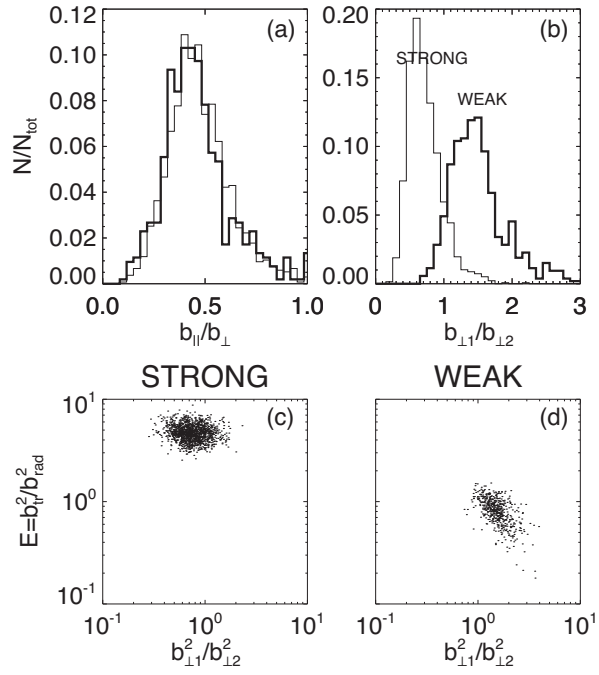

Figure 3. Top panels: distribution in the strong- and weak-expansion data sets (thin and thick lines, respectively) of the ratio between the amplitude of field-parallel and field-perpendicular magnetic fluctuations, $b_\parallel/b_\perp$ (left) and of the amplitudes of magnetic fluctuations in the two field-perpendicular components, $b_{\perp1}/b_{\perp2}$ (right). Bottom panels: scatterplot of $b^2_{\perp1}/b^2_{\perp2}$ versus $E = b^2_{\rm tr}/b^2_{\rm rad}$ for the strong- and weak-expansion data sets in the bottom left and bottom right panels, respectively.

The dark shaded area corresponds to the selection criterion of the weak-expansion data set, $0 < E < 2$. It is clear that the distribution of θ_{BR} is peaked at $\pi/2$ for a given value of the parameter $b_{\perp1}/b_{\perp2}$, but not all values are allowed. If one decreases further the ratio, for $b_{\perp1}/b_{\perp2} < 1/\sqrt{2}$ the minimum value of E is larger than 2 and no interval can satisfy the weak-expansion constraint. When the field-aligned fluctuations are not negligible (right-hand panel for which $b_\parallel/b_{\perp2} = 0.4$), the function becomes asymmetric, the minimum of E increases and shifts to larger angles, but the above considerations remain valid as far $b_\parallel/b_{\perp2} \lesssim 1$. The grey shaded area corresponds to the selection criterion of the strong-expansion data set, $2 < E < 10$. Again the value of $E_{\rm min}$ puts an upper limit to $b_{\perp1}/b_{\perp2} < 1/\sqrt{10}$, for larger value the data set is empty. Requiring $E < 10$ also has the effect of excluding intervals with mean-field almost aligned to the radial direction: the lower the ratio $b_{\perp1}/b_{\perp2}$, the larger the angles that are omitted. However, as the field-parallel fluctuations are non-negligible, intervals with radial mean field direction are no more excluded and smaller ratios of $b_{\perp1}/b_{\perp2}$ are allowed (right-hand panel).

The above constraints on the field-perpendicular components can be seen in the distributions shown in Fig. 3. In the top left panel, one can see that the condition $b_\parallel/b_\perp < 1$ is generally satisfied and the distributions are very similar in both data sets. On the contrary, the value $b_{\perp1}/b_{\perp2} = 1$ roughly separates the distributions in the top right panel, the ratio being generally smaller for strong expansion and larger for weak expansion, with peak values at 0.5 and 1.5, respectively. We also show a scatterplot of E versus the ratio $b^2_{\perp1}/b^2_{\perp2}$ for strong and weak expansion in the bottom left and right panels, respectively. While for strong expansion no correlation can be seen, for the weak expansion a clear anticorrelation appears because of the relation $E_{\rm min} = b^2_{\perp2}/b^2_{\perp1}$ which bounds E from below. In other words, values $b_{\perp1}/b_{\perp2} > 1$ for weak expansion are expected as a consequence of the selection criterion, while for strong expansion the selection criterion puts no constraint on the perpendicular component anisotropy. However, its distribution spans basically values $b_{\perp1}/b_{\perp2} < 1$. A ratio smaller than one can be understood as a consequence of the divergence-less condition for the magnetic field. In fact, the fluctuation $b_{\perp1}$ is perpendicular to B_0 but has a non-vanishing projection on the wavevector k along the radial sampling direction. On the contrary, $b_{\perp2}$ is perpendicular to both B_0 and k. If the two components have the same power and spectral index (α), for an oblique mean field and a sampling along the radial direction the ratio $b^2_{\perp1}/b^2_{\perp2} = 1/\alpha$ at all scales (Saur & Bieber 1999).

To summarize, the combination of three factors determine the ordering in the two data sets of the amplitudes of the components of magnetic fluctuations as seen in the field-aligned reference frame (variance or component anisotropy). These factors are: the selection criterion, the divergence-less constraint of magnetic fluctuation, and the smaller amplitude of field-aligned fluctuations compared to field perpendicular fluctuations (the latter is also a consequence of the divergence-less constraint if energy resides mostly in field-perpendicular wavevectors). For the strong-expansion data set one has $b_\parallel < b_{\perp1} < b_{\perp2}$, while for the weak-expansion data set the ordering of the perpendicular components is reversed, $b_\parallel < b_{\perp2} < b_{\perp1}$. Note that on the one hand, the selection criterion for weak expansion also forces the mean magnetic field to be preferentially perpendicular to the radial direction, and since fluctuations in the BR plane are large, the magnetic field direction is expected to vary substantially (see below). On the other hand, the mean-field direction is much less constrained for the strong-expansion data set and can take basically any value.

3.2 Data set properties, two representative intervals

We now describe the properties of the two data sets, first by inspecting one interval per data set and then by looking at the distributions of the properties of intervals in each data set. The time series of (i) the radial velocity, the magnetic field intensity (left-hand panels), (ii) the three components of velocity and magnetic fluctuations in Alfvén units (black and red lines, respectively, central

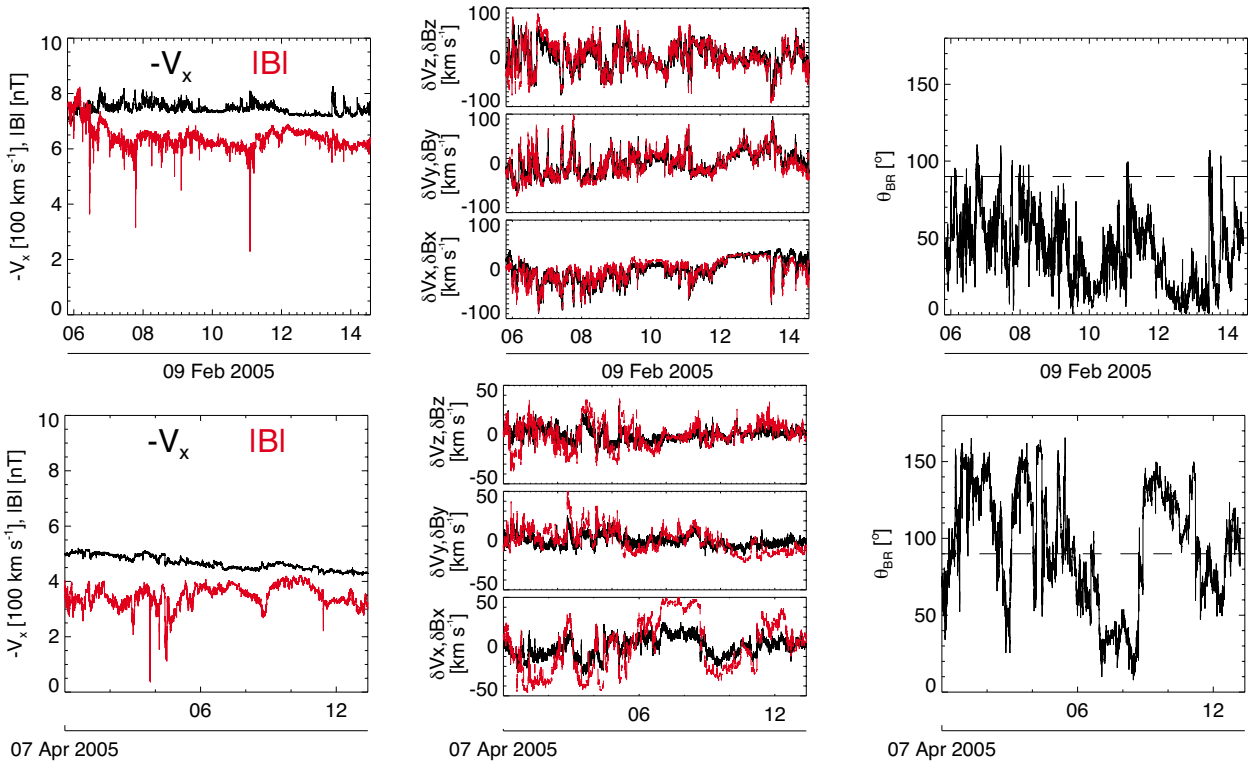

Figure 4. Time series of two intervals representative of the strong-expansion data set (top panels) and weak-expansion data set (bottom panels). Left column: solar wind radial velocity, $V_R = -V_x$ (black), and magnetic field intensity, $|B|$ (red). Central column: components of velocity and magnetic fluctuations, $\delta V_{X,\,Y,\,Z}$ and $\delta B_{X,\,Y,\,Z}$ in black solid and red dashed lines, respectively. Right column: magnetic field angle with respect to the radial direction, θ_{BR}.

panel), and (iii) the angle between the magnetic field and the flow direction, θ_{BR} (right-hand panels), are plotted in Fig. 4 for two intervals representative of the strong-expansion data set (top) and of the weak-expansion data set (bottom).

The strong-expansion interval is a fast stream of average radial speed of $V_R = -V_x \approx 700$ km s^{-1}, on top of which several jets of the order of 50 km s^{-1} are visible (top left panel). Such velocity enhancements are (anti) correlated to the variations of the magnetic intensity (red line) and are related to the Alfvénic nature of this interval. In fact, as can be seen in the central top panel, velocity and magnetic fluctuations are strongly correlated. Note that the X and Y components of the fluctuations are 'one-sided', i.e. asymmetric with respect to zero, a characteristic of Alfvénic fluctuations with constant $|B|$ (Gosling et al. 2009; Matteini et al. 2014), although here $|B|$ is not perfectly constant. The amplitude of fluctuations is larger in the Z component and about the same in the X- and Y components, reflecting the selection criterion $E = b_{\rm tr}/b_{\rm rad} > 2$. Finally, the magnetic field is on average aligned with the Parker spiral (top right panel), it has almost no change in its polarity with variations in the angle θ_{BR} being generally smaller than 45° (only in few cases variations reach 90° and are associated with the jets in the radial velocity).

The weak-expansion interval has a moderate wind speed of about 400 km s^{-1}, with small radial velocity fluctuations, and a weaker and more variable magnetic intensity (bottom left panel). Velocity and magnetic fluctuations are about a factor 2 smaller than in the strong-expansion interval (compare the central panels), they are only weakly correlated and are about symmetric with respect to zero. Magnetic fluctuations (red lines) have larger amplitudes in the X component, again reflecting the selection criterion $E = b_{\rm tr}/b_{\rm rad} < 2$. The magnetic field is now on average perpendicular to the radial direction (the dashed line in the bottom right panel), although the instantaneous direction varies largely, with fluctuations of the order of 90° associated with a change in magnetic field polarity and intensity.

3.3 Distribution of properties in intervals

We finally show how properties related to those just commented above are distributed in the two data sets. For the strong-expansion data set we plot in Fig. 5 the distributions of: (a) the average cross-helicity $\sigma_c = -2\boldsymbol{u}\cdot\boldsymbol{b}/(u^2+b^2)$ calculated with fluctuations in the frequency band $f \in [4.6, 9.2]10^{-4}$ Hz (left-hand panel); (b) the solar wind speed and the skewness of the radial velocity (central panels); and (c) the average magnetic field angle, θ_{BR}, along with its standard deviation, $\Delta\theta_{BR}$ (right-hand panels). Most of the intervals have a large average cross-helicity (left-hand panel), the solar wind speed is almost uniformly distributed with a slight dominance of slow streams (top central panel), and the average angle of the magnetic field is clustered around 50° and 120° (top right panel), the latter being more inclined with respect to the nominal direction of the Parker spiral (indicated by vertical dotted lines). The radial velocity fluctuations are mostly asymmetric, with the distribution of the skewness $SK(V_x)$ having a maximum around −0.4 (central bottom panel), which indicates the presence of one-sided fluctuations as seen in the top panels of Fig. 4 (recall that $V_R = -V_x$). The standard deviation of the magnetic field angle $\Delta\theta_{BR}$ has a narrow distribution (bottom right panel), with a mean value of 20°, so that intervals contain basically no polarity inversion.

In each plot, the thick histograms refer to a subsample of intervals having $|\sigma_c| \geq 0.7$, which represents 57 per cent of the entire sample. Their average solar wind speed spans the entire range of the

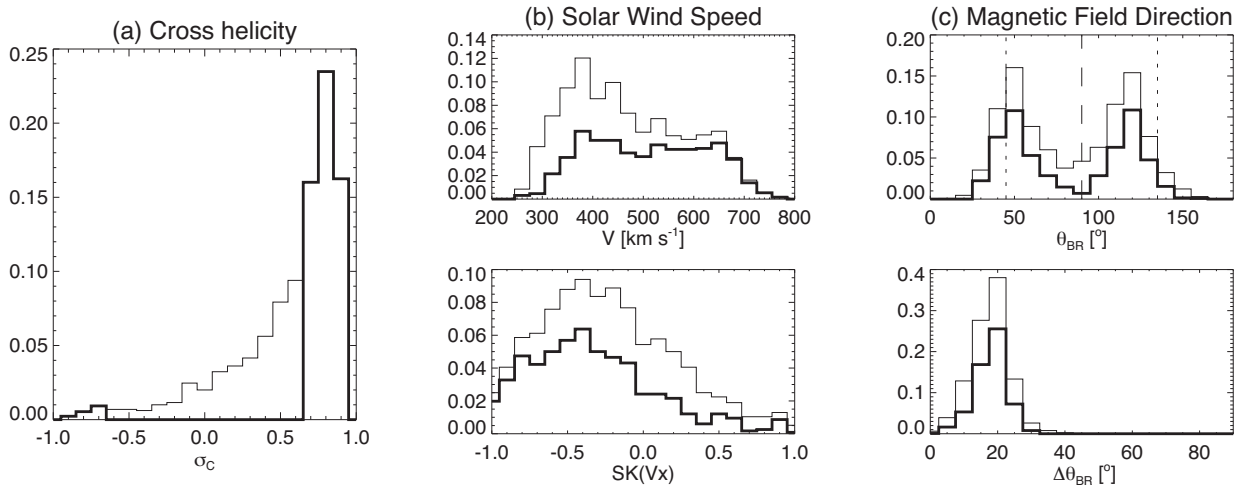

Figure 5. Strong-expansion data set. Distribution of the normalized cross-helicity, σ_c, calculated with fluctuations in the frequency band $f \in [4.6, 9.2]10^{-4}$ Hz (left-hand panel), the mean solar wind speed and the skewness of its radial component, V and $SK(V_x)$ (top and bottom central panels, respectively), the average angle between the magnetic field and the radial direction along with its standard deviation, θ_{BR} and $\Delta\theta_{BR}$ (top and bottom right panels, respectively). The thick histograms refer to a subsample with $|\sigma_c| \geq 0.7$.

distribution, reflecting the presence of classical fast and Alfvénic streams, along with the slow and Alfvénic streams recently analysed in D'Amicis, Matteini & Bruno (2018). The Alfvénic streams also contribute mostly to the asymmetry of the fluctuations in V_x. The remainder of the population is made up of slow streams with small Alfvénicity and a flat distribution of the radial velocity skewness.

In Fig. 6 we plot the distribution of the same quantities for the weak-expansion data set. The data set contains mostly non-Alfvénic fluctuations (left-hand panel), embedded in slow streams (top central panel), and the mean field is preferentially perpendicular to the radial direction (top right panel). The distribution of $\Delta\theta_{BR}$ is broad and has an average value of $\sim 30^o$ (left bottom panel). At variance with the strong data set, the mean field direction varies substantially within a given interval. Finally, the distribution of the skewness of the radial velocity has a maximum around zero and an important secondary peak at negative values. Asymmetric radial velocity fluctuations are also contained in this data set (central bottom panel).

In the same figure, thick lines refer to distributions that are limited to a subsample with large cross-helicity, $|\sigma_c| \geq 0.7$, which represents only the 27 per cent of the entire sample. This population of Alfvénic fluctuations contains fast and slow streams in about the same proportion, it has a slight asymmetry in the radial velocity fluctuations, but it conserves the properties related to the magnetic field direction: a perpendicular mean field with a large variation of its direction within an interval.

We conclude that the two data sets can be distinguished according to the mean magnetic field direction, its variability within an interval, and by the ratio $b_{\perp 1}/b_{\perp 2}$, rather than by the distribution of cross-helicity, although the strong-expansion data set is mainly associated with Alfvénic fluctuations while the weak-expansion data set contains mostly non-Alfvénic fluctuations.

4 RESULTS

We first analyse the anisotropy of magnetic and velocity structure functions, indicated in the next section with $SF_{B,V}$, respectively. We then study the 3D anisotropy of velocity fluctuations by relaxing the assumption of axisymmetry in the definition of the structure functions, SF (we drop the subscript, the same analysis for magnetic fluctuations can be found in Verdini et al. 2018a). In the following we will also measure the spectral index of SF. We recall that when the Fourier spectrum is a power law in the whole range, $E \propto k^{-\gamma}$, then also the SF is a power law, $SF \propto \ell^{\alpha} \propto k^{-\alpha}$, and its index is related to that of the Fourier spectrum by $\alpha = \gamma - 1$.

4.1 Axisymmetric anisotropy

In Fig. 7 we plot the axisymmetric raw structure functions (see equation 14) of the magnetic and velocity fluctuations for the strong and weak data sets, in the top and bottom panels, respectively, as a function of the wavenumber $k = 1/\ell$. As a reference, in the top x-axis we also indicate the corresponding frequency scale, obtained using an average solar wind speed of 400 km s^{-1}. The magnetic structure functions, SF_B, are multiplied by a factor 10 to separate them from the velocity structure functions, SF_V, the black and red lines indicate the perpendicular and parallel SF, respectively. For both data sets, SF_B has a steeper slope in the parallel direction than in the perpendicular one, while for SF_V the slope is approximately the same in the parallel and perpendicular directions. Without applying any normalization before averaging among intervals belonging to the same data set, SF_V has a power-law index that is independent of θ_{BV}. This is reminiscent of the results of Wang et al. (2014), but note that they averaged the slopes measured in seven fast streams intervals, so that a more appropriate comparison requires a proper normalization in our data set (see below).

In the same figure we also plot, with a dashed line, an evaluation of the noise associated with the quantization of velocity measurement. Following Wicks et al. (2013), we first estimate the error on velocity measurements as the quadratic mean of the most probable value of the velocity increment at 3s in each interval (about 2 km s^{-1} for the radial component and 1.5 km s^{-1} for the other components), and then propagate this error in the definition of SF. The perpendicular SF_V is always larger than the noise level, but only by a factor 2 at the smallest scales. Instead, the noise becomes at least half of the signal in SF_V at *parallel* scales smaller than 8 Mm for strong expansion and smaller than 25 Mm for weak expansion, respectively. A scale of 10 Mm approximately corresponds to

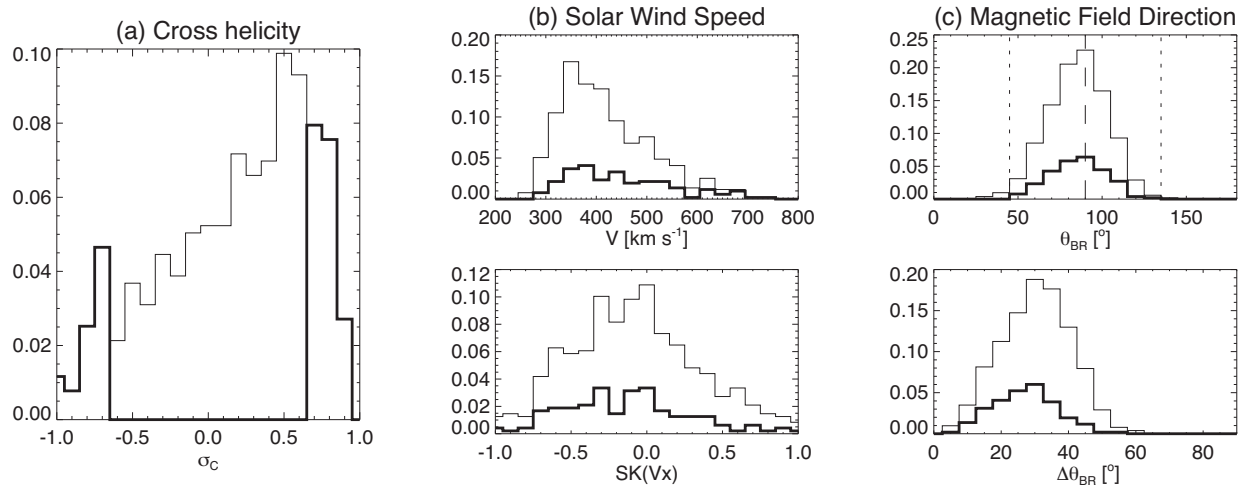

Figure 6. Weak-expansion data set. Same as in Fig. 5 with the thick histograms referring to a subsample with $|\sigma_c| \geq 0.7$.

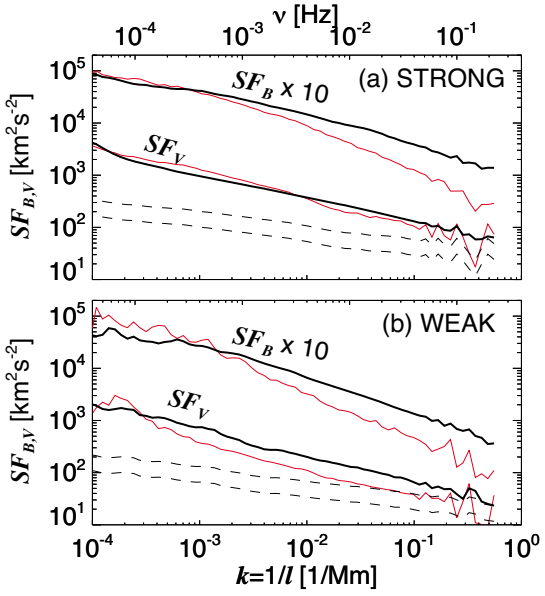

Figure 7. Raw axisymmetric SF of velocity fluctuations (SF_V, bottom lines) and magnetic fluctuations (SF_B, upper lines) obtained by averaging, without any normalization, the SF_i of each interval in the strong (a) and weak (b) data sets (see definition in equation 14). The perpendicular and parallel SF are drawn with thick black and thin red lines, respectively. The noise level on velocity fluctuations is plotted with a dashed line, along with twice its value (upper dashed line). In the top axis we indicate the frequencies corresponding to the length scale in the bottom axis, by assuming an average solar wind speed of 400 km s^{-1}.

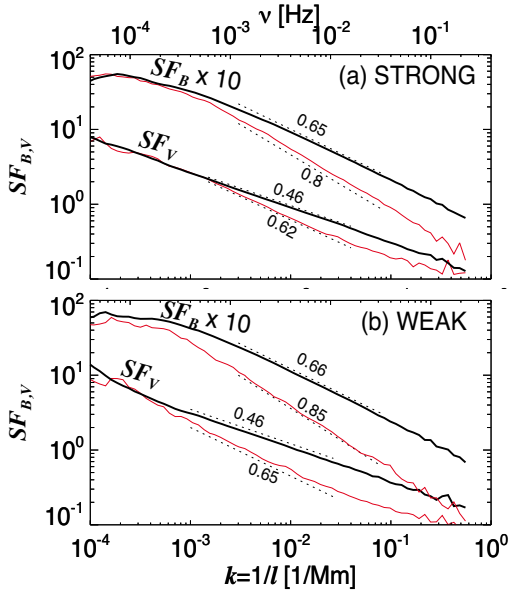

Figure 8. Normalized axisymmetric SF of velocity fluctuations (see equation 12) in the same format as in Fig. 7. The dotted lines are drawn as reference for the power-law scaling $SF \propto k^{-\alpha}$ with the index α indicated in the figure.

a frequency of $f = 4 \times 10^{-2}$ Hz, which is close to the value estimated in Wicks et al. (2013) for the noise to become important.

In Fig. 8 we plot again the axisymmetric SF for magnetic and velocity fluctuations, this time applying a normalization at scale $\ell^* \approx 100$ Mm (see equation 12). One obtains a clearer power-law behaviour compared to the raw SF in Fig. 7, and, more importantly, SF_V now has a dependence on θ_{BV} in both data sets, with larger spectral indices in the parallel directions, in the range $k \in [2 \times 10^{-3}, 4 \times 10^{-2}]$ Mm^{-1} for strong expansion and $k \in [10^{-3}, 2 \times 10^{-2}]$ Mm^{-1} for weak expansion. At larger k the parallel SF_V has approximately the same scaling of the perpendicular SF_V, possibly reflecting the small signal-to-noise ratio at those scales. Note that a different scaling in parallel and perpendicular directions for both $SF_{B,V}$ shows up at larger scales in the bottom panel, indicating that the approximate criterion used to minimize expansion effects works fairly well.

In the same figure we also indicate the values of the spectral index α, measured by fitting $SF \propto k^{-\alpha}$ in the interval indicated by the dotted lines. The spectral indices of the perpendicular $SF_{B,V}$ are the same independent of the strength of expansion, with a Kolmogorov-like index $\alpha_\perp \sim 0.65$ for SF_B and an Iroshinikov–Kraichan-like index, $\alpha_\perp \sim 0.46$ for SF_V, very close to the average values found in observations for Fourier spectra. The parallel spectral indices have a weak dependence on the strength of expansion, passing from $\alpha_\parallel \sim 0.8$ to $\sim$0.85 for magnetic fluctuations, and from $\alpha_\parallel \sim 0.62$ to

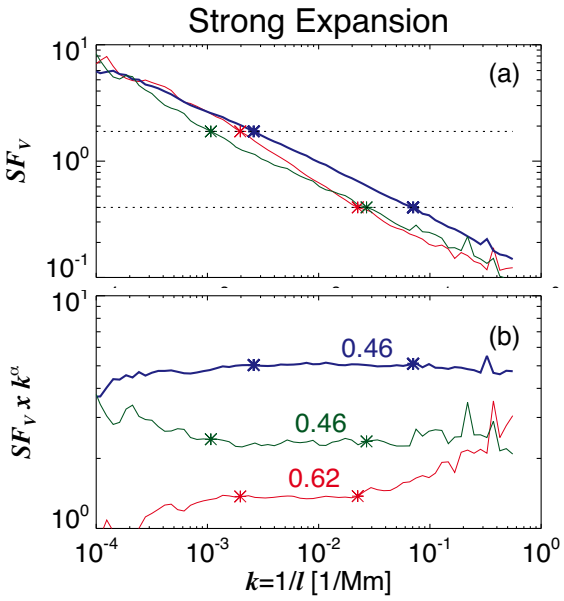

Figure 9. Strong-expansion data set. Panel (a): structure function of velocity fluctuations along the three orthogonal axes of the local reference frame (see Fig. 1): the perpendicular, displacement, and parallel directions are drawn with thick blue, green, and thin red lines, respectively. Panel (b): the same three directions are now compensated by the power-law indices measured in the range $SF \in [1.5, 5]$ (delimited by asterisks on each line) and indicated on top of each line. The lines are vertically shifted by an arbitrary factor for better visualization.

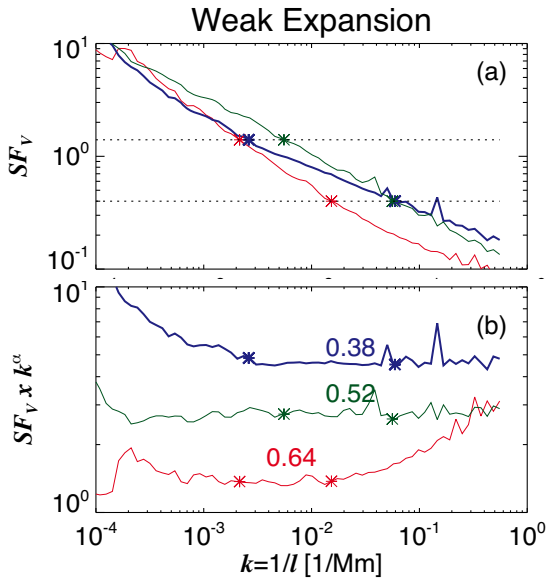

Figure 10. Weak-expansion data set. Same format as in Fig. 9.

$\sim$0.65 for velocity fluctuations when expansion is weaker. Note that at variance with Wang et al. (2014) we obtain parallel SF_V that are steeper than the perpendicular SF_V, but the parallel spectral index is much smaller than the value 1 found by Wicks et al. (2011).

4.2 Three-dimensional anisotropy

In Fig. 9a we plot the structure functions of the velocity fluctuations, now indicated by *SF*, for the strong-expansion data set, in the three orthogonal directions, the perpendicular, displacement, and parallel directions ($\ell_\perp$, $L_\perp$, and $\ell_\parallel$ in blue, green, and red, respectively) that are defined as:

$$SF(\ell_\perp) \rightarrow (85^o < \theta_B < 90^o, 85^o < \phi_{\delta B\perp} < 90^o), \quad (17)$$

$$SF(L_\perp) \rightarrow (85^o < \theta_B < 90^o, 0^o < \phi_{\delta B\perp} < 5^o), \quad (18)$$

$$SF(\ell_\parallel) \rightarrow (0^o < \theta_B < 5^o, 0^o < \phi_{\delta B\perp} < 90^o). \quad (19)$$

The parallel and perpendicular *SF*s have the same energy at large scales, a marker for strong expansion (Verdini & Grappin 2015). For $k \gtrsim 10^{-3}$ Mm^{-1} the parallel *SF* has a steeper slope and becomes subdominant at small scales, while the perpendicular and displacement *SF*s become parallel to each other. At very small energies the parallel *SF* (red line) starts to flatten, as already seen in the axisymmetric *SF* in Fig. 8a. The precise scaling laws in the three orthogonal directions are shown in Fig. 9b where the the *SF* are compensated by the power-law index measured in the energy interval $0.4 \lesssim SF \lesssim 1.5$ (marked by asterisks in both panels and indicating our fiducial inertial range). The two perpendicular *SF*s have a slope of 0.46 while the parallel *SF* has a steeper slope, close to 0.62. The inequality $SF(\ell_\perp) > SF(L_\perp)$ suggests that power anisotropy is a consequence of the large-scale component anisotropy, $b_{\perp 1}/b_{\perp 2} < 1$ seen in Fig. 3b. In fact, on the one hand, $SF(\ell_\perp)$ is measured when the local mean field direction is along $b_{\perp 2}$, and $SF(L_\perp)$ is measured when the local field direction is along $b_{\perp 1}$. On the other hand, because of the strong Alfvénicity, velocity fluctuations are expected to be almost incompressible and hence subject to the divergence-less constraint. Indeed also the their large-scale fluctuations have a component anisotropy with a ratio $v_{\perp 1}/v_{\perp 2} < 1$ (not shown).

In Fig. 10 we plot the *SF* in the three directions for the weak-expansion data set, also compensating them by the power-law index measured in the range $0.4 \lesssim SF \lesssim 1.5$ (delimited by asterisks on the lines and representative of the inertial range). The displacement *SF* is the most energetic at almost all scales, reflecting the large-scale component anisotropy $b_{\perp 1}/b_{\perp 2} > 1$ already seen in Fig. 3b. This inequality is induced by the selection criterion for the weak-expansion data set and implies that fluctuations are preferentially aligned with the radial direction, which is when $SF(L_\perp)$ is measured. In the inertial range, the *SF* has now three distinct slopes in the perpendicular, displacement, and parallel directions, with indices 0.38, 0.52, and 0.64, respectively. Below the bottom dashed line, i.e. for energies $\lesssim$0.4, the *SF* is spiky, an indication that we are possibly reaching the noise in the measurements.

The shape of turbulent eddies can be visualized in Fig. 11, where we draw the isosurfaces of constant energy of the *SF* at three different levels, $SF \approx 1.5$, 0.4, and 0.2, corresponding to smaller and smaller scales. The isosurface can be thought of as the average shape of a turbulent eddy with given energy, as viewed in the varying frame attached to the local mean magnetic field. For strong expansion (left-hand panels), at the energy corresponding to the top boundary of the power-law interval in Fig. 9, the eddy is mostly elongated in the displacement direction and is about isotropic in the parallel and perpendicular directions (top left panel). At intermediate energies (central left panel), corresponding to the bottom boundary of the power-law interval, the eddy is thinning in the perpendicular direction, which is now the smallest dimension,

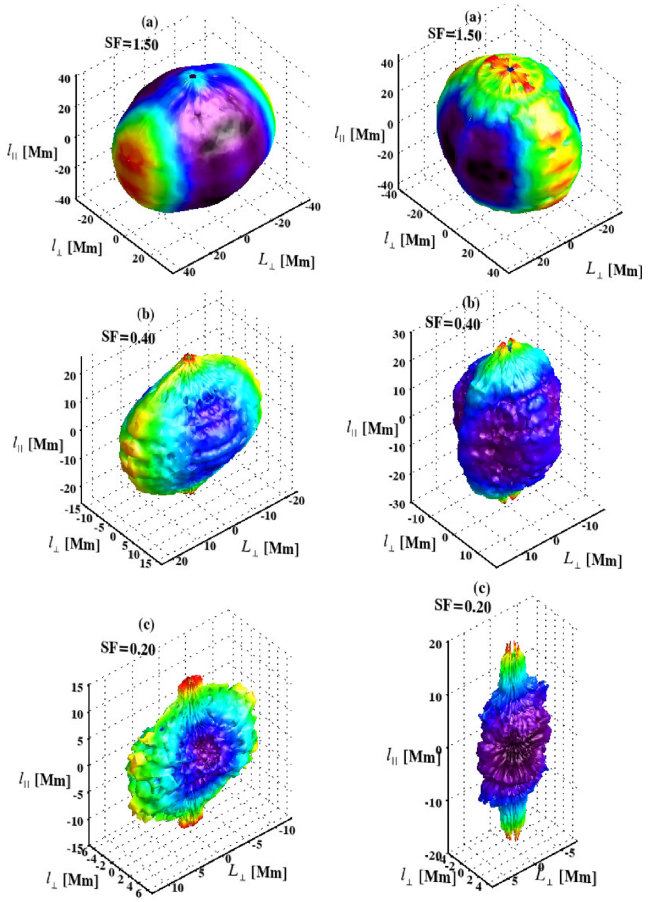

Figure 11. Strong-expansion data set (left) and weak-expansion data set (right). Isosurface of constant energy of the velocity structure function at three different levels, $SF \approx 1.5$, 0.4, 0.2, in panels (a), (b), and (c), respectively. The colour is redundant, it indicates the distance from the centre for better visualization.

and becomes isotropic in the parallel and displacement directions. At the smallest energy and scales (bottom left panel) the structure is again thinner in the perpendicular direction and maintains an approximate isotropy in the parallel and displacement directions, although a larger elongation in the parallel direction begins to appear.

In Fig. 9a one can see that the ratio $SF(\ell_\perp)/SF(L_\perp) \sim 1.5$ at all scales. If SF is measured in a fixed reference frame (global anisotropy) and the sampling direction is not aligned with the mean field direction, Saur & Bieber (1999) have shown that for an axisymmetric spectrum made of field-perpendicular fluctuations and wavevectors, the ratio of power in the the two components is $P_{\perp 1}/P_{\perp 2} = 1/\alpha$, because of the divergence-less condition of magnetic fluctuations. Although this argument applies only for measurements in a fixed reference frame, it strongly suggests that two local structure functions, $SF(\ell_\perp)$ and $SF(L_\perp)$, actually have the same power.[1] If this is roughly true, all the eddy shapes shown in the left column should be squeezed in the $L_\perp$ direction. Thus, the small-scale shape that is similar to a disc would be consistent with a tube-like structure.

In the right column of Fig. 11, we give the same 3D representation for the weak-expansion data set. At the largest scales (top right panel), structures are again axisymmetric around the displacement direction, but the eddy is thinner along the axis of symmetry. At the bottom boundary of the inertial range (central right panel) one sees already a tendency to bi-dimensionalization, with the main axis along the parallel direction and approximate axisymmetry. At very small scales (bottom right panel), the eddy is clearly bi-dimensional with the main axis along the mean field and sheet-like, with a strong aspect ratio in the perpendicular plane, consistent with the different scaling in the perpendicular and displacement direction seen in Fig. 10. We conclude by noting that at the smallest scales (bottom panels), the eddies have dimensions comparable or smaller than 10 Mm, which is the scale at which the signal-to-noise ratio falls below 2 (see Fig. 7), thus casting doubts on their utility. We decided to show them because their shape is very similar to the one obtained with magnetic fluctuations (not shown, but see Verdini et al. 2018a for the weak-expansion data set), which have much higher resolution and are not contaminated by noise.

5 SUMMARY AND DISCUSSION

We have studied the local anisotropy of velocity fluctuations in two previously identified data sets in which expansion effects are expected to be small and large, respectively. The selection criterion is $0 < E < 2$ for weak expansion and $2 < E < 10$ for strong expansion, with E being the ratio of the energy in transverse and radial components of magnetic fluctuations calculated at 2 h scale, $E = b_{\rm tr}^2/b_{\rm rad}^2$. For strong expansion, the mean field direction is clustered around the Parker spiral and fluctuations are mainly Alfvénic, with a strong correlation between magnetic and velocity fluctuations. For weak expansion, the mean field direction is preferentially perpendicular to the radial direction (a consequence of the selection criterion) and magnetic and velocity fluctuations are weakly correlated. When no distinction is made between the two field-perpendicular directions, i.e. axisymmetry around the mean field is assumed, the two data sets have very similar distributions of the magnetic field compressibility, $b_\parallel/b_\perp < 1$. Also the axisymmetric local anisotropy as measured by structure functions, SF, is very similar.

Let us denote with $\alpha_{\parallel,\perp}$ the power-law index $SF \sim k^{-\alpha}$ in the (local) parallel and perpendicular directions, respectively. For magnetic fluctuations, we find $\alpha_\perp \sim 0.65$, 0.66 and $\alpha_\parallel \sim 0.8$, 0.85 in the strong- and weak-expansion data sets, respectively. Note that the difference in parallel and perpendicular spectral indices is slightly larger and appears at larger scales in the weak-expansion data set, suggesting that the criterion used to limit expansion effects works fairly well despite being approximate (see Vech & Chen 2016 for the relative contribution of expansion and the divergence-less constraint on the ratio E). These results are consistent with previous findings (e.g. Horbury et al. 2008; Podesta 2009; Luo & Wu 2010; Wicks et al. 2010, 2011), although the parallel index is significantly smaller than 1, a value expected for strong turbulence subject to the critical balance between the linear Alfvén time and the eddy turnover time (Goldreich & Sridhar 1995; Boldyrev 2005, 2006). Small values of $\alpha_\parallel$ were obtained when intermittency was explicitly removed from the data (Wang et al. 2014) or when requiring

[1]We recall that $SF(\ell_\perp)$ is measured when the sampling direction is perpendicular to both the fluctuation and the mean field and it can be loosely associated with $P_{\perp 2}$. Instead, $SF(L_\perp)$ is measured when fluctuations have non-vanishing projection in the sampling direction and can be loosely associated with $P_{\perp 1}$. In addition, in this data set, fluctuations are mainly Alfvénic so that also the velocity fluctuations are also expected to have vanishing divergence.

the stationarity of the mean field direction (Wang et al. 2016), which also indirectly limits intermittency. We have not measured intermittency in our data sets, and it seems unlikely that the selection criterion limits intermittency in the selected intervals. Instead, our results are consistent with a small $\alpha_\parallel$ resulting from a non-negligible contribution of the slab component (von Papen & Saur 2015). Such component is mostly observed in fast wind streams with Alfvénic fluctuations, a population that is more abundant in the strong-expansion data set, which actually displays a flatter parallel *SF* than for weak expansion.

For velocity fluctuations the indices are generally smaller, with $\alpha_\perp \sim 0.46$, 0.46 and $\alpha_\parallel \sim 0.62$, 0.65 in the strong- and weak-expansion data sets, respectively. At variance with Wicks et al. (2013), the parallel index is much smaller than 1 and it is consistent with the value found by Wang et al. (2014) upon removal of intermittency from the data. As already said, it seems unlikely that intermittency is absent in our data and other explanations are needed. A possibility is that the parallel *SF* is contaminated by noise in the velocity measurements that is different from the quantization noise estimated here, further work is needed to clarify this issue.

It is curious that $\alpha_\parallel$ and $\alpha_\perp$ of velocity *SF* are related to each other by the critical balance between Alfvén time and a non-linear time, when the latter is based on velocity fluctuations. By equating the two time-scales defined as $\tau_A = \ell_\parallel/V_A$ and $\tau_{NL} = \ell_\perp/v(\ell_\perp)$, respectively, and using the scaling $SF(\ell_\perp) \sim \ell_\perp^{1/2}$ seen in Fig. 9, one obtains $SF(\ell_\parallel) \sim \ell_\parallel^{2/3}$ which is very close to the measured parallel scaling. This is suggestive of a turbulent regime in which the cascades of magnetic and kinetic energies proceed independently. On the one hand, such a regime would contrast with the cascade of ideal invariants, since in incompressible MHD only the sum of the two energies is an invariant, and also with the strong Alfvénicity of fluctuations in the strong-expansion data set. On the other hand, different spectral indices for the magnetic and velocity fluctuations are routinely found in numerical simulations (Milano et al. 2001; Müller & Grappin 2004; Boldyrev, Perez & Wang 2012; Grappin et al. 2016), which indicates a sort of decoupling between the two fields, with a magnetic excess naturally developing at large scales and in the inertial range (Grappin et al. 1983; Muller & Grappin 2005; Boldyrev & Perez 2009). Very recently it has been shown that when kinetic energy is injected at large scales, the transfer to magnetic energy stops to be effective at small scales in the inertial range, called the inductive range (Bian & Aluie 2019). In this range of scales, the cascades of kinetic and magnetic energy decouple and attain the same rate, thus supporting the above regime, although it is not clear yet if the independent cascades are associated with separate spectral indices for magnetic and kinetic energy.

When axisymmetry is relaxed, differences in the two data sets emerge. Consider first the properties of fluctuations at large scales, which are used to characterize the data sets. Because of the small magnetic compressibility, $b_\parallel/b_\perp < 1$, the selection criterion for weak expansion have two implications: (i) intervals have a mean field preferentially perpendicular to the radial direction; (ii) the field-perpendicular component lying in the *BR* plane has a larger amplitude than the field-perpendicular component orthogonal to the *BR* plane, $b_{\perp 1}/b_{\perp 2} > 1$ (see Fig. 3b). The selection criterion for the strong-expansion data set puts no constraint on the mean field direction and on ratio of the field-perpendicular components. The distribution of the magnetic field angle with the radial, θ_{BR}, is thus clustered around the Parker spiral direction. However we find that $b_{\perp 1}/b_{\perp 2} < 1$. This inequality is opposite to that of the weak-expansion data set and can be understood as a consequence of the divergence-less constraint for b when the mean field is not aligned to the (radial) sampling direction (Saur & Bieber 1999). Thus, the two data sets have different large-scale variance anisotropy, $b_\parallel < b_{\perp 1} < b_{\perp 2}$ for strong expansion and $b_\parallel < b_{\perp 2} < b_{\perp 1}$ for weak expansion.

The 3D *SF* of velocity fluctuations also have distinctive features in the two data sets. For strong expansion the perpendicular and displacement *SF* have the same spectral index, $\alpha = 0.65$, with smaller power in the displacement *SF*. This is due to the large-scale variance anisotropy $b_{\perp 1} < b_{\perp 2}$ and the Alfvénic character of fluctuations (see discussion in Section 4.2). The constant ratio of the two perpendicular *SF* at all scales suggests that the smaller power in the displacement *SF* is an observational bias that hides an actual axisymmetry around the mean field as shown by Saur & Bieber (1999). Although the relation $SF(\ell_\perp)/SF(L_\perp) = 1/\alpha$ holds only when anisotropy is computed in a fixed reference frame (global anisotropy), it is likely that a similar effect occurs for the local anisotropy analysed here.

For weak expansion, we find a non-axisymmetric anisotropy: the perpendicular *SF* is flatter than the displacement *SF*, their indices being $\alpha = 0.38$, 0.52, respectively. However, because the large-scale variance anisotropy, $b_{\perp 1} > b_{\perp 2}$, the displacement *SF* has more power than the perpendicular *SF*. This implies that when axisymmetry is assumed, the perpendicular *SF* takes the power-law index of the displacement *SF*, which explains why the axisymmetric anisotropy is the same in both data sets. The resulting eddy shape, as measured by isosurfaces of constant energy, is also different in the two data sets. As a rule, at smaller and smaller scales, eddies become more elongated in the direction of the local magnetic field in both data sets. However, while for strong expansion the small-scale structure of eddies is consistent with an axisymmetric tube-like shape, for weak expansion it is more similar to a ribbon (although the latter correspondence is not strict because of the large power in the displacement *SF*).

The 3D anisotropy of magnetic fluctuations in the same data sets was analysed in Verdini et al. (2018a) who found similar properties. For strong expansion, the two perpendicular *SF*s have the same index $\alpha = 0.65$, while for weak expansion $\alpha = 0.53$, 0.74 in the perpendicular and displacement *SF*s, respectively. The former are in agreement with earlier measurement in the fast polar wind (Chen et al. 2012), and can be interpreted in light of the similar properties of the strong-expansion data set: Alfvénic fluctuations with a large-scale component anisotropy, $b_{\perp 1} < b_{\perp 2}$. The latter are instead associated with the opposite component anisotropy, $b_{\perp 1} > b_{\perp 2}$, and to the mean magnetic field being perpendicular to the radial direction. In conclusion, we have shown that the measurement of the 3D local anisotropy for both magnetic and velocity fluctuations is largely influenced by the underlying large-scale variance anisotropy of the magnetic fluctuations, as already pointed out in numerical simulations of MHD turbulence with expansion (Verdini & Grappin 2015).

Our results confirm that the difference in the magnetic and velocity spectral indices is a solid property that shows up whether we compare Fourier spectra, or parallel and perpendicular axisymmetric *SF*, or non-axisymmetric *SF*. This is somehow paradoxical, since magnetic and velocity fluctuations exhibit a strong coupling as measured by the cross-helicity ($2\delta\boldsymbol{v}\cdot\delta\boldsymbol{b}/|\delta\boldsymbol{b}^2+\delta\boldsymbol{v}^2|$) or by the alignment of magnetic and velocity fluctuations ($\delta\boldsymbol{v}_\perp\cdot\delta\boldsymbol{b}_\perp/|\delta\boldsymbol{b}_\perp||\delta\boldsymbol{v}_\perp|$), but at the same time the two fields can have decoupled cascades (Bian & Aluie 2019). A local measure of the alignment angle in the same data sets used here is reported in Verdini et al. (2018b). Although the progressive alignment with scales stops at relatively large scales, the angle remains small (∼23°) in the weak-expansion data set (see

also Podesta et al. 2009; Wicks et al. 2013, for similar results). Such an alignment suggests a strong (non-linear) coupling between velocity and magnetic fluctuations, which indeed have qualitatively similar anisotropies. However, this measure puts no constraint on the relative amplitudes of the two fields. Instead, Chen et al. (2013) found that for strongly Alfvénic intervals, the magnetic spectral index approaches that of velocity fluctuations with value −3/2. We find here a slope consistent with −5/3 in the strong-expansion data set, where most of the intervals have $\sigma_c > 0.7$, and the same index is reported by Chen et al. (2012) that analysed fast streams with $\sigma_c \approx 0.6$. This indicates that only very large values of cross-helicity ($|\sigma_c| > 0.9$) cancel the difference in spectral index between velocity and magnetic spectra, i.e. alignment alone is not enough and equipartition between the two fields must also hold.

Recent numerical simulations (Yang et al. 2017) and data analysis (Wang et al. 2014, 2016; Bowen et al. 2018) suggest that the differences in spectral indices are related to a stronger intermittency level in magnetic fluctuations, possibly due to the presence of pressure-balance structure in the solar wind. Intermittency correction should steepen the magnetic spectrum, but there is no particular reason for the resulting slope to be −5/3. Moreover, when intermittency is removed from data so as to obtain a monofractal behaviour of the exponent in higher order two-point correlations (Salem et al. 2009), the spectral indices of magnetic and velocity fluctuations remain basically unchanged. We have not analysed intermittency in our data sets, but in view of the above considerations on alignment and equipartition between velocity and magnetic fluctuations, our results seem to support an alternative scenario in which the spectral indices are regulated by a scale-by-scale equilibrium between the tendency to magnetic and kinetic equipartition (linear Alfvén effect) and the generation of magnetic excess (non-linear local dynamo) (Grappin et al. 1983; Müller & Grappin 2004; Muller & Grappin 2005; Grappin et al. 2016), with possibly a large-scale driver as expansion. However, again there is no particular reason for the indices of magnetic and kinetic spectra to be −5/3 and −3/2, respectively. Understanding this property remains one of the most challenging achievement in solar wind turbulence.

ACKNOWLEDGEMENTS

This work has been done within the LABEX PLAS@PAR project, and received financial state aid managed by the Agence Nationale de la Recherche, as part of the Programme 'Investissements d'Avenir' under the reference ANR-11-IDEX-0004-02. RG and OA acknowledge support from Programme National PNST of CNRS/INSU co-funded by CNES. *Wind* data were obtained from CDAWeb (http://cdaweb.gsfc.nasa.gov).

REFERENCES

Beresnyak A., 2015, ApJ, 801, L9
Beresnyak A., Lazarian A., 2006, ApJ, 640, L175
Bian X., Aluie H., 2019, Phys. Rev. Lett., 122, 135101
Bieber J. W., Wanner W., Matthaeus W. H., 1996, J. Geophys. Res., 101, 2511
Boldyrev S., 2005, ApJ, 626, L37
Boldyrev S., 2006, Phys. Rev. Lett., 96, 115002
Boldyrev S., Perez J. C., 2009, Phys. Rev. Lett., 103, 225001
Boldyrev S., Perez J. C., Borovsky J. E., Podesta J. J., 2011, ApJ, 741, L19
Boldyrev S., Perez J. C., Wang Y., 2012, in Pogorelov N. V., Font J. A., Audit E., Zank G. P., eds, ASP Conf. Ser., Vol. 459, Numerical Modeling of Space Plasma Flows. Astron. Soc. Pac., San Francisco, p. 3
Bowen T. A., Mallet A., Bonnell J. W., Bale S. D., 2018, ApJ, 865, 45
Bruno R., Carbone V., 2013, Living Rev. Sol. Phys., 10, 2
Chen C. H. K., Mallet A., Schekochihin A. A., Horbury T. S., Wicks R. T., Bale S. D., 2012, ApJ, 758, 120
Chen C. H. K., Bale S. D., Salem C. S., Maruca B. A., 2013, ApJ, 770, 125
Cho J., Vishniac E. T., 2000, ApJ, 539, 273
D'Amicis R., Matteini L., Bruno R., 2018, MNRAS, 483, 4665
Dasso S., Milano L. J., Matthaeus W. H., Smith C. W., 2005, ApJ, 635, L181
Dong Y., Verdini A., Grappin R., 2014, ApJ, 793, 118
Franci L., Verdini A., Matteini L., Landi S., Hellinger P., 2015a, ApJ, 804, L39
Franci L., Landi S., Matteini L., Verdini A., Hellinger P., 2015b, ApJ, 812, 21
Franci L., Hellinger P., Matteini L., Verdini A., Landi S., 2016, in Wang L., Bruno R., Mobius E., Vourlidas A., Zank G., eds, 14th International Solar Wind Conference (Solar Wind), American Institute of Physics, USA, p. 040003
Gerick F., Saur J., von Papen M., 2017, ApJ, 843, 5
Ghosh S., Matthaeus W. H., Roberts D. A., Goldstein M. L., 1998a, J. Geophys. Res., 103, 23691
Ghosh S., Matthaeus W. H., Roberts D. A., Goldstein M. L., 1998b, J. Geophys. Res., 103, 23705
Goldreich P., Sridhar S., 1995, ApJ, 438, 763
Gosling J. T., McComas D. J., Roberts D. A., Skoug R. M., 2009, ApJ, 695, L213
Grappin R., 1986, Phys. Fluids, 29, 2433
Grappin R., Muller W.-C., 2010, Phys. Rev. E, 82, 26406
Grappin R., Velli M., 1996, J. Geophys. Res., 101, 425
Grappin R., Leorat J., Pouquet A., 1983, A&A, 126, 51
Grappin R., Velli M., Mangeney A., 1993, Phys. Rev. Lett., 70, 2190
Grappin R., Müller W.-C., Verdini A., 2016, A&A, 589, A131
Hamilton K., Smith C. W., Vasquez B. J., Leamon R. J., 2008, J. Geophys. Res., 113, A01106
Heinemann M., 1980, J. Geophys. Res., 85, 3435
Horbury T. S., Forman M., Oughton S., 2008, Phys. Rev. Lett., 101, 175005
Krstulovic G., Brachet M. E., Pouquet A., 2014, Phys. Rev. E, 89, 043017
Lacombe C., Alexandrova O., Matteini L., 2017, ApJ, 848, 45
Lee E., Brachet M. E., Pouquet A., Mininni P. D., Rosenberg D., 2010, Phys. Rev. E, 81, 016318
Lepping R. P. et al., 1995, Space Sci. Rev., 71, 207
Lin R. P. et al., 1995, Space Sci. Rev., 71, 125
Luo Q. Y., Wu D. J., 2010, ApJ, 714, L138
Mason J., Cattaneo F., Boldyrev S., 2006, Phys. Rev. Lett., 97, 255002
Mason J., Cattaneo F., Boldyrev S., 2008, Phys. Rev. E, 77, 036403
Matteini L., Horbury T. S., Neugebauer M., Goldstein B. E., 2014, Geophys. Res. Lett., 41, 259
Matthaeus W. H., Lamkin S. L., 1986, Phys. Fluids, 29, 2513
Matthaeus W. H., Goldstein M. L., Roberts D. A., 1990, J. Geophys. Res., 95, 20673
Matthaeus W. H., Ghosh S., Oughton S., Roberts D. A., 1996, J. Geophys. Res., 101, 7619
Meyrand R., Galtier S., Kiyani K. H., 2016, Phys. Rev. Lett., 116, 105002
Milano L. J., Matthaeus W. H., Dmitruk P., Montgomery D. C., 2001, Phys. Plasmas, 8, 2673
Montagud-Camps V., Grappin R., Verdini A., 2018, ApJ, 853, 153
Montgomery D., Turner L., 1981, Phys. Fluids, 24, 825
Müller W.-C., Grappin R., 2004, Plasma Phys. Control. Fusion, 46, B91
Müller W.-C., Grappin R., 2005, Phys. Rev. Lett.., 95, 114502
Müller W.-C., Biskamp D., Grappin R., 2003, Phys. Rev. E, 67, 066302
Narita Y., Glassmeier K.-H., Sahraoui F., Goldstein M. L., 2010, Phys. Rev. Lett., 104, 171101
Osman K. T., Matthaeus W. H., Greco A., Servidio S., 2011, ApJ, 727, L11
Osman K. T., Matthaeus W. H., Hnat B., Chapman S. C., 2012, Phys. Rev. Lett., 108, 261103
Oughton S., Matthaeus W. H., Wan M., Parashar T., 2016, J. Geophys. Res., 121, 5041

Papini E., Franci L., Landi S., Verdini A., Matteini L., Hellinger P., 2019, ApJ, 870, 52
Perez J. C., Mason J., Boldyrev S., Cattaneo F., 2012, Phys. Rev. X, 2, 041005
Perrone D., Alexandrova O., Mangeney A., Maksimovic M., Lacombe C., Rakoto V., Kasper J. C., Jovanovic D., 2016, ApJ, 826, 196
Perrone D., Alexandrova O., Roberts O. W., Lion S., Lacombe C., Walsh A., Maksimovic M., Zouganelis I., 2017, ApJ, 849, 49
Podesta J. J., 2009, ApJ, 698, 986
Podesta J. J., Roberts D. A., Goldstein M. L., 2007, ApJ, 664, 543
Podesta J. J., Chandran B. D. G., Bhattacharjee A., Roberts D. A., Goldstein M. L., 2009, J. Geophys. Res., 114, A01107
Roberts O. W., Narita Y., Escoubet C. P., 2017, ApJ, 851, L11
Salem C., Mangeney A., Bale S. D., Veltri P., 2009, ApJ, 702, 537
Saur J., Bieber J. W., 1999, J. Geophys. Res., 104, 9975
Shebalin J. V., Matthaeus W. H., Montgomery D., 1983, J. Plasma Phys., 29, 525
Tessein J. A., Smith C. W., MacBride B. T., Matthaeus W. H., Forman M. A., Borovsky J. E., 2009, ApJ, 692, 684
Vech D., Chen C. H. K., 2016, ApJ, 832, L16
Velli M., Grappin R., Mangeney A., 1992, in Spicer D. S., MacNeice P., eds, American Institute of Physics Conference Series Vol. 267, workshop on Electromechanical Coupling of the Solar Atmosphere, AIP Press, Woodbury. p. 154
Verdini A., Grappin R., 2012, Phys. Rev. Lett., 109, 025004
Verdini A., Grappin R., 2015, ApJ, 808, L34
Verdini A., Grappin R., 2016, ApJ, 831, 179
Verdini A., Grappin R., Hellinger P., Landi S., Müller W. C., 2015, ApJ, 804, 119
Verdini A., Grappin R., Alexandrova O., Lion S., 2018a, ApJ, 853, 85
Verdini A., Grappin R., Alexandrova O., Lion S., 2018b, ApJ, 867, 168
Völk H. J., Aplers W., 1973, Ap&SS, 20, 267
von Papen M., Saur J., 2015, ApJ, 806, 116
Wang X., Tu C., He J., Marsch E., Wang L., 2014, ApJ, 783, L9
Wang X., Tu C., Marsch E., He J., Wang L., 2016, ApJ, 816, 15
Weygand J. M., Matthaeus W. H., Dasso S., Kivelson M. G., Kistler L. M., Mouikis C., 2009, J. Geophys. Res. , 114, A07213
Weygand J. M., Matthaeus W. H., Dasso S., Kivelson M. G., 2011, J. Geophys. Res., 116, A08102
Wicks R. T., Horbury T. S., Chen C. H. K., Schekochihin A. A., 2010, MNRAS, 407, L31
Wicks R. T., Horbury T. S., Chen C. H. K., Schekochihin A. A., 2011, Phys. Rev. Lett., 106, 45001
Wicks R. T., Roberts D. A., Mallet A., Schekochihin A. A., Horbury T. S., Chen C. H. K., 2013, ApJ, 778, 177
Yang L., He J., Tu C., Li S., Zhang L., Wang X., Marsch E., Wang L., 2017, ApJ, 846, 49
Zank G. P., Adhikari L., Hunana P., Shiota D., Bruno R., Telloni D., 2017, ApJ, 835, 147

This paper has been typeset from a TEX/LATEX file prepared by the author.